Atomic physics on a 50-nm scale: Realization of a bilayer system of dipolar atoms

Atomic physics on a 50-nm scale: Realization of a bilayer system of dipolar atoms

Li Du[*,†], Pierre Barral[†,‡], Michael Cantara[†,§], Julius de Hond[†,¶], Yu-Kun Lu, and Wolfgang Ketterle
Research Laboratory of Electronics, MIT-Harvard Center for Ultracold Atoms, and Department of Physics, Massachusetts Institute of Technology, Cambridge, Massachusetts 02139, USA
(Dated: May 1, 2024)

Controlling ultracold atoms with laser light has greatly advanced quantum science. The wavelength of light sets a typical length scale for most experiments to the order of 500 nanometers (nm) or greater. In this work, we implemented a super-resolution technique that localizes and arranges atoms on a sub–50-nm scale, without any fundamental limit in resolution. We demonstrate this technique by creating a bilayer of dysprosium atoms and observing dipolar interactions between two physically separated layers through interlayer sympathetic cooling and coupled collective excitations. At 50-nm distance, dipolar interactions are 1000 times stronger than at 500 nm. For two atoms in optical tweezers, this should enable purely magnetic dipolar gates with kilohertz speed.

A major frontier in many-body physics is the realization and study of strongly-correlated quantum phases [1–3]. In ultracold atomic systems, the typical short-range contact interaction has led to the creation of a variety of exotic quantum phases [3, 4]. However, a wide range of quantum phenomena require long-range dipolar interactions [5–7]. But even for the most magnetic atoms such as chromium, erbium and dysprosium (Dy), the magnetic dipole-dipole interaction is rather weak. For Dy, with a magnetic dipole moment of 10 Bohr magneton (μ_B), the dipolar interaction at 500-nm distance is only $h \times 20$ Hz, where h is the Planck's constant. Although such weak interactions could be observed [8, 9], and supersolidity and other forms of matter could be realized with magnetic atoms [5], there are major efforts to harness the much stronger interactions of polar molecules [10, 11] and Rydberg atoms [12]. The electric dipolar interaction of molecules (at 3 D) can be 1000 times stronger than magnetic dipolar interaction (at 10 μ_B). In this work, we show how this factor of 1000 can be compensated for by decreasing the distance between two magnetic atoms to 50 nm. Studying dipolar physics with neutral atoms has major advantages: It is simpler to cool atoms to quantum degeneracy, and atoms have more favorable collisional properties.

It has been a long-standing goal to create optical potentials with subwavelength components to enhance tunneling and interaction strengths. Early works on atom lithography achieved deposition of metal structures with spatial periods one-eighth the size of optical wavelengths [13, 14] and feature sizes of tens of nanometers [15] using state-dependent potentials. With ultracold atoms, many schemes have been suggested [16–20] and methods such as dark states [21, 22], radio frequency-photon dressing [23], stroboscopic techniques [24], and multiphoton processes through Raman transitions between hyperfine states [13, 25, 26] have been demonstrated. Challenges, such as additional heating, limited coherence time, and limited reduction of atomic spacing, have hindered a wide adoption of these methods. In this work, we introduce a method that has no fundamental limit. It is based on the key concept of optical super-resolution microscopy: One can determine the center of a diffraction-limited Airy disk with a precision that exceeds the diffraction limit. Similarly, a deep optical lattice or a strong tweezer beam can localize an atom to 10 nm [15, 27, 28], limited only by available power and heating from spontaneous light scattering. In a typical super-resolution microscopy experiment, molecules are imaged sequentially, whereas for trapping atoms, simultaneous confinement on a subwavelength scale is required. One possible solution is to trap two different kinds of atoms with two different colors of light. But, usually, for quantum science, one needs identical atoms. The strategy we implemented was to use two opposite spin states of Dy, and two different polarizations of light at different frequencies — a dual-polarization and dual-frequency super-resolution scheme. Unlike spin-1/2 and alkali atoms, ground-state Dy has a strong tensor polarizability [29]. It can cause detrimental two-photon Raman couplings between spin states with different m_J quantum numbers, which are suppressed by the frequency offset between the two optical potentials. The remaining diagonal part of the tensor couplings makes our scheme much more robust since it creates, for ^{162}Dy, an isolated two-state Hilbert space for $m_J = \pm 8$ spin states with a big energy gap to all the other 15 spin states.

Spin-dependent potentials have been realized with rubidium [30–34] and cesium [27, 35]. In contrast to alkali atoms [36], very deep spin-dependent potentials can be realized with Dy with negligible spontaneous emission as a result of Dy's electronic orbital angular momentum in the ground state. Furthermore, with a magnetic dipole moment of only 1 μ_B, the dipolar

* Corresponding author. Email: lidu@mit.edu;
† These authors contributed equally to this work.;
‡ Present address: Amazon Web Services, Boston, MA, USA.;
§ Present address: Oracle Cloud Infrastructure, Boston, MA, USA.;
¶ Present address: PASQAL SAS, Fred. Roeskestraat 100, Amsterdam, Netherlands.

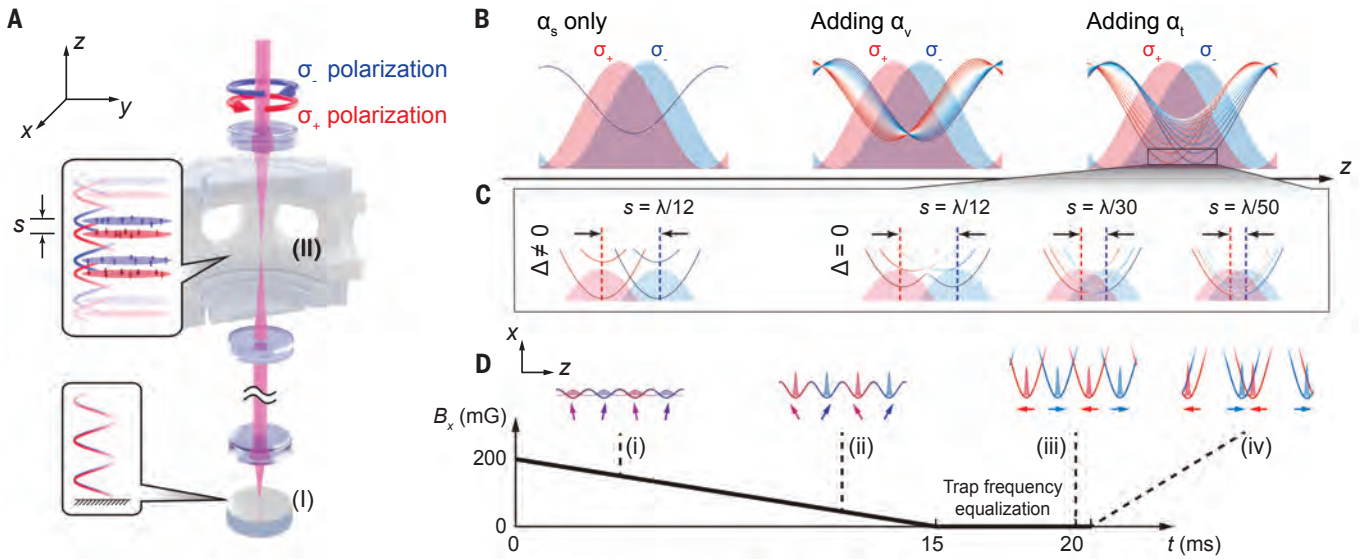

FIG. 1. **Creation of the subwavelength bilayer array.** (**A**) Experimental setup. Two overlapping laser beams with opposite circular polarizations σ_+ and σ_- are retro-reflected by mirror (I) to form two optical standing waves. The two standing waves are displaced at the position of the atoms (II), which is controlled by the frequency offset Δ between the two laser beams. Dy atoms in this configuration form an array of pancake-shaped bilayers of head-to-head dipoles with adjustable interlayer distance s. (**B**) Contributions of different polarizability components. Solid lines denote adiabatic potential curves for different m_J states ($-8 \leq m_J \leq 8$, represented by dark blue to dark red, assuming red detuning), and the shaded regions refer to the intensities of the $\sigma_\pm$ light for a particular interlayer separation. (**C**) If the two laser beams have the same frequency $\Delta = 0$, the off-diagonal part of the tensor polarizability mixes spin states. As a result, the two minima merge into a single minimum for small separation s. This is avoided in our experiment by using two different frequencies for the $\sigma_\pm$ light. The color of the curves indicate the m_J character of the adiabatic eigenstates. (**D**) Adiabatic loading of the bilayer array. (i) Starting with the optical potential in the interlaced configuration in the presence of a dominating transverse magnetic field $B_x = 200$ mG, the atoms are initialized in the $m_J = -8$ spin state along the x direction. (ii) As B_x is ramped down in 15 ms, the light shift dominates over the Zeeman shift, thereby adiabatically loading the bilayer array. (iii) The power of the σ_+ and σ_- potentials is adjusted for identical trap frequencies. (iv) The interlayer distance is adjusted to designated values in 0.5 ms.

interaction for alkali atoms is 100 times weaker than for Dy. Therefore, previous work on alkalis has used spin-dependent forces to control the overlap between sites with spin up and down [27, 33] but not to study interactions between nonoverlapping sites.

The subwavelength scheme

An illustration of the experimental scheme is shown in Fig. 1B, which demonstrates a bilayer potential created by two optical standing waves of σ_+ and σ_- polarizations with a small spatial spatial displacement s. This illustration also applies to the case of spin-dependent optical tweezers. The figure shows the adiabatic potentials of all 17 spin states (quantized along the z direction in the lab frame), with different polarizability components taken into account. With only a scalar polarizability α_s, the ac Stark shifts are the same for all 17 m_J states, so there is only one potential minimum. The vector polarizability α_v leads to ac Stark shifts that are linear in m_J and therefore can be regarded as a Zeeman shift caused by a fictitious sinusoidal magnetic field — it lifts the degeneracy except for points where the fictitious magnetic fields from the σ_+ and the σ_- standing waves cancel. This creates a double well potential even for arbitrarily small displacement of the standing waves. However, small transverse magnetic fields would couple the degenerate states, leading to mixing among different m_J states. This is where the tensor polarizability α_t makes a qualitative difference. The diagonal part of the tensor light-atom interaction (which has an m_J^2 dependence) partially lifts the degeneracy. The $m_J = \pm 8$ ground states are separated from all other states by a large gap and are coupled by transverse fields only in 16th order. Note that the $m_J = \pm 8$ states are the local ground states of the $\sigma_\pm$ potential minima, and therefore inelastic two-body losses are prevented in each of the layers.

Although the tensor polarizability α_t provides robustness against transverse magnetic fields, it allows for two-photon Raman processes with $\Delta m_J = \pm 2$ using one σ_+ and one σ_- photon. Figure 1C shows the effect of the resonant Raman process caused by off-diagonal tensor couplings when both polarization components have the same frequency. This is the situation when the σ_+ and the σ_- standing waves are created by retro-reflecting a single beam with rotated linear polarization, as often used for alkalis (e.g., see [30, 31, 33]). For Dy, the Raman couplings weaken the potential minima for separa-

tions smaller than $\lambda/10$, where λ is the wavelength of the light. For displacements of the standing waves of less than $\lambda/30$, the double minima have merged. We eliminated the Raman coupling by offsetting the frequencies for the σ_+ and σ_- optical standing waves by more than 300 MHz, much larger than the ac Stark shifts, which makes the two-photon Raman process off-resonant [37]. The conclusion is that the dual-polarization and dual-frequency scheme isolates the Hilbert space for the $m_J = \pm 8$ spin states and creates a double-minimum potential that is not flattened out even for very small separations of the two minima.

Dy, with its high angular momentum of $J = 8$ in the ground state, is the ideal atom for this scheme. For a $J = 8 \rightarrow J' = 9$ transition, the $m_J = 8$ state has a transition strength ratio of 153 between the σ_+ and σ_- transitions [38]. For atoms with $J = 1$ (2), the ratio is only 6 (15). Therefore, this stretched transition in Dy is very similar to a hypothetically isolated $J = 1/2 \rightarrow J' = 1/2$ transition, where the spin-up state sees only σ_- light and vice versa. Dy is even more ideal than the $J = 1/2$ case in which spin-up and down states are directly connected by possible one- or two-body couplings (e.g. transverse magnetic fields, dipolar relaxation), whereas those couplings act only in 16th or 8th order in our Dy scheme. The robustness of the scheme comes from the ac Stark shifts that stem from the tensor polarizability.

Experimental protocol

Experimentally, we created a stack of bilayers by superimposing red-detuned optical standing waves with σ_+ and σ_- polarizations operating near the Dy narrowline transition at 741 nm (linewidth $\Gamma/2\pi = 1.78$ kHz) [39]. The two optical beams were delivered through the same polarization-maintaining fiber, such that they shared the same transverse Gaussian mode. The frequency of the σ_- standing wave can be dynamically tuned using a double-passed phased-array acousto-optic deflector, leading to a precise control of the interlayer distance s with a sensitivity of 4.7 nm/MHz [see Supplementary Materials (SM)].

The ground state of the bilayer was loaded using an adiabatic transfer method, as depicted in Fig. 1D. First, $m_J = -8$ atoms were prepared in a magnetic field with a transverse component $B_x = 200$ mG and an axial component B_z around 10 mG. We then ramped up the σ_+ and σ_- standing waves in the interlaced configuration with $s = \lambda/4$ in 100 ms, loading all layers with atoms aligned with the x axis (Fig. 1D, i). By ramping down B_x in 15 ms, the potential depth increased while a bilayer array was formed with dipoles aligned head to head (Fig. 1D, ii and iii). We ensured balanced loading by making sure that the energy offset (including Zeeman energies) between the minima of the σ_+ and σ_- potentials was zero. It was crucial that the atoms stayed in their local ground state throughout the experiment to prevent losses and heating caused by dipolar relaxation. Therefore, the Zeeman shifts caused by the external magnetic field B_z had to be smaller than the differential ac Stark shift between the $m_J = -8$ and $m_J = -7$ states.

After loading a balanced bilayer array, the powers of the two optical standing waves were ramped up, ensuring that the two layers had the same trap frequencies of typically $(\omega_x, \omega_y, \omega_z) = 2\pi \times (0.5, 0.5, 140)$ kHz. The strong axial confinement resulted in a harmonic oscillator length $a_{\mathrm{HO}} = \sqrt{\hbar/m\omega_z}$ of 21.1 nm, where $\hbar = h/2\pi$ and m is the atomic mass. We loaded 4.2×10^4 ultracold ^{162}Dy atoms into an array of 42 bilayers, with a temperature of 1.7 μK determined from the cloud size after ballistic expansion (see SM) [40]. Subsequently, the interlayer distance s was ramped from $\lambda/4$ to different designated values in 0.5 ms by changing the frequency of the σ_- standing wave. The interlayer distance s was calibrated with Kapitza-Dirac diffraction measurements (see SM). At the end of each experimental sequence, the atoms were released from the bilayer array within 1 μs and were imaged after ballistic expansion. With the small axial magnetic field B_z serving as a guiding field, atoms remained in the $m_J = \pm 8$ states and were imaged by a spin-resolved absorption imaging technique (see SM). This method allowed us to measure the population in each of the two layers simultaneously.

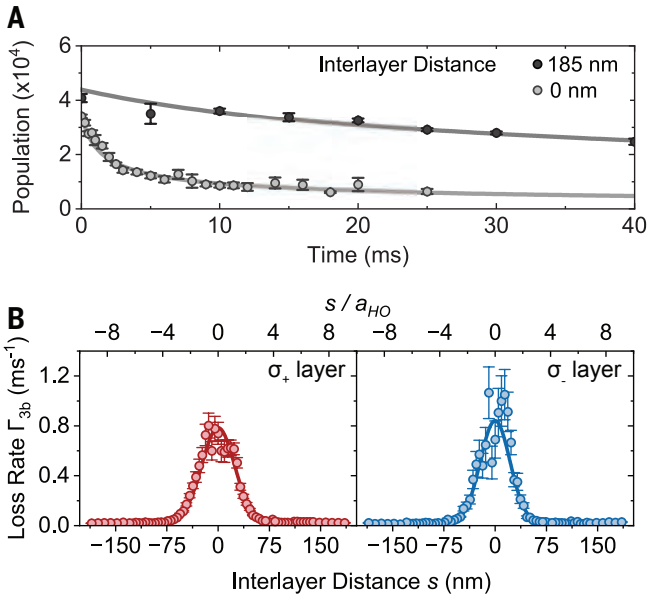

FIG. 2. **Subwavelength control of the interlayer distance, as demonstrated by recording atom loss as a function of layer separation.** (**A**) Evolution of the population in σ_+ layers at two different interlayer distances $s = 185$ nm and 0 nm. The loss is much faster when the layers are overlapped. Initial loss rates Γ_{3b} are obtained from the fits to the decay curves. (**B**) Gaussian fits of the initial loss rates Γ_{3b} to the interlayer distances s according to Eq. (1) (solid lines) provide a value of $\sigma_z = 19 \pm 1$ nm for the layer thickness.

Demonstration of spatial control

We demonstrated the subwavelength spatial control over the bilayer geometry by measuring the lifetime of atomic samples at different layer separations. The sharp peak in the loss rate as a function of interlayer distance s in Fig. 2 is essentially the convolution between the density profiles of the two layers. Assuming that loss processes occur at short range, we derived a rate equation for the total loss rate Γ_{3b} of each layer

$$\Gamma_{3b} = \Gamma_{\text{intra}} + \Gamma_{\text{inter}} e^{-\frac{1}{3}(\frac{s}{\sigma_z})^2} = \frac{\dot{N}_{\text{tot}}}{N_{\text{tot}}} \qquad (1)$$

where N_{tot} is the total number of atoms in a layer and σ_z is the root-mean-square thickness of each layer. The loss rate contains both an intra- and an interlayer contribution characterized by Γ_{intra} and Γ_{inter}. The factor of one-third in the exponent of the interlayer term reflects that the loss is caused by three-body recombination (see SM). For spin-independent three-body collisions and thermal clouds, we expect that $\Gamma_{\text{intra}} = \Gamma_{\text{inter}}$. Unexpectedly, we observed about a 50-fold increase in the loss rate when the two layers were overlapped, which implies that three-body recombination involving mixed spin states is much faster than recombination of three atoms all in the same spin state. This strongly enhanced loss feature serves as a highly sensitive monitor for the density overlap between the two layers; fitting the loss curve determines the thickness of each layer $\sigma_z = 19 \pm 1$ nm, consistent with the calculated value of $1.31 a_{\text{HO}}/\sqrt{2} \approx 18.8 \pm 0.1$ nm that we obtained from trap frequency and temperature measurements [40]. The observed losses in the two layers are almost equal, which implies equal loss rates for three-body collisions involving one spin-up and two spin-down atoms, or vice versa. This measurement of the atomic density distribution has no discernible broadening: The measured and calculated widths agreed to within 1 nm. Expressing this as an instrumental point spread function gives an upper limit to the Gaussian width of the point-spread function of 6 nm. This result can be compared with what was achieved in dark-state super-resolution microscopy. McDonald *et al.* [22] measured an atom cloud size of 55 nm with a broadening of 32 nm due to the width of the dark-state probe. A similar experiment reported by Subhankar *et al.* [41] measured a size of 26 nm with a broadening of 11 nm from the probe.

We conclude from the loss measurement that the two layers can be regarded as coupled predominantly by long-range dipolar forces for $s \gtrapprox 50$ nm. The dipolar energy U_{dd}/h between two Dy atoms with opposite spins at this separation is 20 kHz. This geometry now allows us to study dipolar physics with strong interlayer dipole-dipole interactions.

Interlayer thermalization

We applied our technique to study energy transfer through interlayer dipolar interactions, or sympathetic cooling between two atomic systems separated by vacuum [42, 43]. Each layer receives heat through the fluctuating magnetic field created by the dipoles in the other layer. For equal temperatures, in detailed balance, the heat flows cancel. For unequal temperatures, the dipolar fluctuations cause thermalization. Figure 3B shows the experimental results.

We experimentally created a controlled temperature difference between the two layers by heating up the σ_+ layer through a parametric drive by modulating the σ_+ light intensity at twice the transverse trap frequency for 30 ms, followed by a 5-ms hold to ensure any residual breathing motion is damped out. This procedure prepares the σ_+ layer at 3.9 μK and leaves the σ_- layer

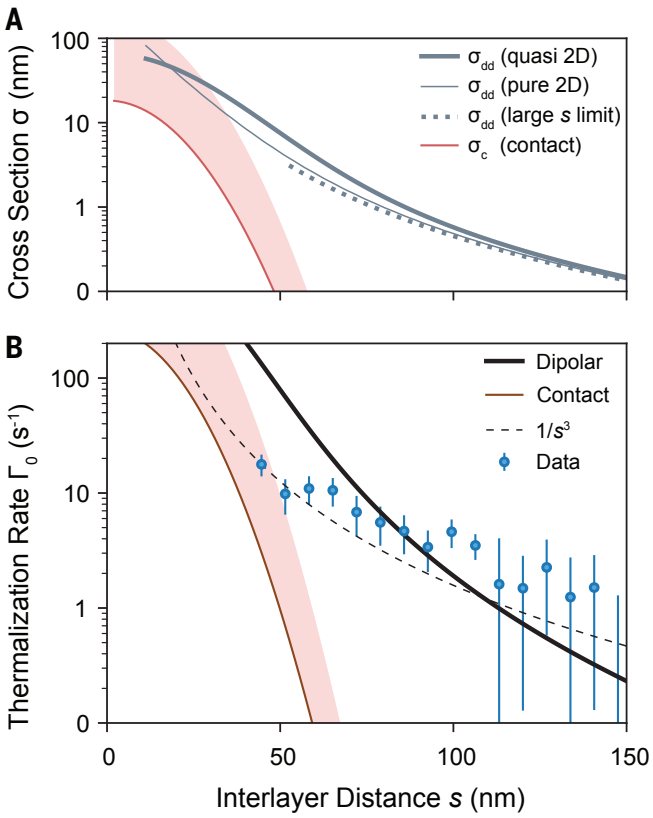

FIG. 3. **Observation of interlayer thermalization.** (**A**) Interlayer elastic scattering cross sections as functions of separation s calculated using the Born approximation. The grey curves correspond to dipolar cross sections for infinitely thin $\sigma_z = 0$ layers (thin grey) along with its large interlayer distance limit $ks \gg 1$ (dashed, following Eq. 2) and for layers with finite thickness $\sigma_z = 14.9$ nm (quasi 2D, solid grey). The red curve is for simple contact interactions at the background scattering length (red, quasi 2D), and the shaded area corresponds to a 10-times-enhanced cross section. (**B**) Observed thermalization rates Γ_0 obtained from the pseudo-exponential fits. The black and red solid lines show the expected thermalization rate from dipolar and contact interactions (see SM). The dashed line is for reference and is proportional to $1/s^3$. Error bars represent the standard errors of the rates obtained from the pseudo-exponential fits.

at 1.7 μK. We then adjusted the interlayer distance over 0.5 ms and monitored the temperature evolution. We fit the temperature difference between two layers to a pseudo-exponential decay $\frac{\mathrm{d}\Delta T}{\mathrm{d}t} = -\Gamma_0 \frac{N(t)}{N(0)}\Delta T$ to obtain the interlayer thermalization rate Γ_0, where $N(t)$ accounts for the measured particle number decay caused by inelastic collisions (see SM). Figure 3B shows that the thermalization rate strongly drops with interlayer distance.

We could estimate the interlayer collision rate as $n_{2D}\sigma_{dd}v_{rel}$, where n_{2D} is the 2D density distribution and σ_{dd} is the cross section for two dipolar atoms passing each other at the separation s. Using the Born approximation, we calculated the elastic cross section between two atoms in thin layers separated by a distance s (see SM), and the analytic large-s limit is

$$\sigma_{dd}^{2D} = a_{dd}^2 \frac{\pi}{k^2 s^3} \tag{2}$$

Here, $a_{dd} = 10.2$ nm is the dipolar length and k is the relative momentum between the colliding particles. For $s = 75$ nm, the quasi-2D cross section σ_{dd} is 0.38 nm (see Fig. 3A). With a typical 2D peak density of $n_{2D} \approx 1.3 \times 10^9$ cm^{-2} and a thermal velocity of 2.1 cm s^{-1} one obtains an interlayer collision rate of 100 s^{-1}. The observed thermalization times are much slower, around 160 ms (rate of 6 s^{-1}). This can be fully accounted for by the anisotropy of dipolar scattering peaked in the forward direction, which reduces the effective cross section by a factor of six, and by multiple averaging arising from the inhomogeneity of our sample (see SM). In Fig. 3B, we compare the observed thermalization rates to calculations (see SM). They do not have any adjustable parameters and fully take into account the momentum and angular dependence of dipolar scattering and the finite thickness of the layer. The calculations are in semiquantitative agreement with the observations. The drop-off of the thermalization rate is much weaker than the steep exponential decrease in density overlap and, therefore, in the contact interactions between the two layers. This is clear evidence for purely dipolar collisions in the range of 50- to 100-nm interlayer distances.

The observed dependence on s roughly follows a $1/s^3$ dependence, which is less steep than predicted. This is possibly a consequence of the assumption of purely dipolar binary collisions. For small s, there can be an interference term with s-wave contact interactions and a contribution from nonuniversal short-range dipolar s-wave scattering [44], which is not included in the Born approximation. The largest separations s studied are comparable to the interparticle separation, and the binary collision approximation may no longer be accurate; that is, there are now more then two particles interacting with each other.

Coupled collective oscillations

In the second experiment, we looked for coupled collective oscillations of the bilayer system. Several theoretical papers [45, 46] predicted the coupling of transverse oscillations by the mean dipolar field between the layers. Indeed, when we excited transverse oscillations in one layer, we found that they caused oscillations in the other layer (Fig. 4). Experimentally, after loading a balanced bilayer array and adjusting the interlayer distance to a designated value in 0.5 ms, we adiabatically displaced the σ_+ layer along the transverse direction y in 10 ms using an extra laser beam with σ_+ polarization. This beam, blue-detuned from the 626-nm transition by 458 MHz, is misaligned from the atoms by about one beam waist and displaces the atoms only in the σ_+ layer (see SM). A sudden switch-off of this beam hence creates a center-of-mass oscillation of the σ_+ layer at the transverse trap frequency with an adjustable amplitude ranging from 0 to 8 μm, depending on the final power of the beam. As a function of hold time, we obtained the in-trap velocity of each layer from time-of-flight images to reveal how momentum is transferred between layers.

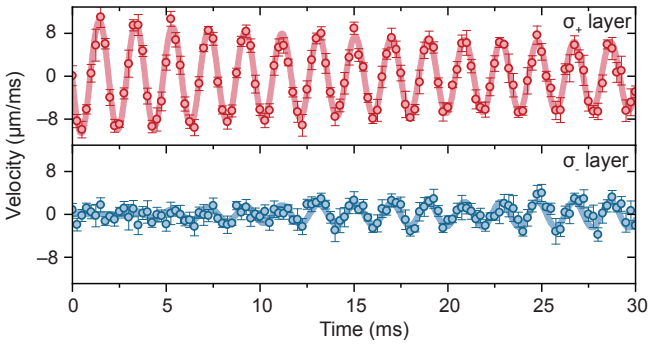

FIG. 4. **Observation of coupled oscillations of the two layers at 62 nm interlayer distance.** The center-of-mass oscillation of the σ_+ layer is excited by suddenly switching off a displacement force. The σ_- layer oscillates because of dipolar coupling. Error bars represent the standard errors of the means of independent measurements.

Figure 4 shows the time evolution of the velocity of each layer at $s = 62$ nm, as obtained from ballistic expansion images. The harmonic oscillation of the σ_+ layer shows damping, whereas the σ_- layer starts at rest and shows a growing in-phase oscillation. Our observation contrasts with the theoretical treatments [45, 46], where the mean-field coupling potential would cause a beat note, which is initially an oscillation 90° out of phase. Furthermore, the predicted mean-field coupling [45, 46] resulted in a normal-mode splitting of less than 1 Hz, which is too slow to be observed on the experimental time scale. Our observation is fully consistent with a friction force caused by dipolar collisions: The time constant for the damping of the relative motion between the two layers of 25 ms is similar to the observed interlayer thermalization times. These observations establish dipolar drag between two physically separated layers, which have features in common with Coulomb

drag studied in bilayer semiconductors [47].

Discussion and outlook

We expect that the technique we developed here should work for all atoms that have electronic orbital angular-momentum in the ground state and allow strong vector and tensor ac Stark shifts at sufficiently far detuning. Although it requires the two layers to be in different spin states, those states can be tilted by a transverse magnetic field to angles within 20°. A modified scheme with an in-plane quantization axis could realize attractive interactions and interlayer pairing [7, 48].

Looking ahead, lower temperatures should lead to strong correlations between the layers beyond a mean-field description. Adding transverse optical lattices to the layers will create large repulsive interaction energies between pairs on the same lattice site [7] but can also realize a system described by attractive interactions between particles and holes analogous to electron-hole pairs in bilayer excitons [49]. It is possible to project separate arbitrary potentials into the σ_+ and σ_- layers, which could realize twisted bilayer potentials [50] and more general geometries, including quasi-crystals. These geometries should allow the study of many phenomena that have been predicted for interacting bilayers [7, 45, 46, 51–57]. Applying the super-resolution technique to optical tweezers will allow the study of super-radiance and radiative shifts at separations much smaller than the optical wavelength as well as the study of magnetic interactions and spin exchange between two isolated atoms, which was done recently with polar molecules [58–61]. The tweezer setup can be generalized to a linear array of atoms alternating in spin-up and spin-down states. Moving the spin-up atoms back and forth would provide full connectivity along the chain and realize a spin chain with strong magnetic coupling between nearest neighbors. These ideas can be generalized to higher dimensions.

Acknowledgments
We thank A. Jamison, J. Yang, J. Lyu, and T. De Coninck for experimental assistance and discussions, and J. Xiang and A. Jamison for comments on the manuscript. **Funding:** We acknowledge support from the NSF through grant nos. 1506369 and PHY-2208004, the Center for Ultracold Atoms (an NSF Physics Frontiers Center) through grant no. PHY-1734011, a Vannevar-Bush Faculty Fellowship(grant no. N00014-16-1-2815), and an Army Research Office (ARO) Defense University Research Instrumentation Program (DURIP) grant (no. W911NF-22-1-0024). **Author contributions:** L.D., P.B., M.C. designed and constructed the experimental setup, L.D., P.B., M.C., J.d.H., Y.-K.L. carried out the experimental work. W.K. initiated the work. All authors contributed to the development of models, data analysis and writing of the manuscript. **Competing interests:** None declared.

[1] B. Keimer and J. Moore, The physics of quantum materials, Nature Physics **13**, 1045 (2017).
[2] E. Y. Andrei and A. H. MacDonald, Graphene bilayers with a twist, Nature Materials **19**, 1265 (2020).
[3] M. Lewenstein, A. Sanpera, and V. Ahufinger, *Ultracold Atoms in Optical Lattices: Simulating quantum many-body systems* (OUP Oxford, 2012).
[4] I. Bloch, J. Dalibard, and W. Zwerger, Many-body physics with ultracold gases, Reviews of Modern Physics **80**, 885 (2008).
[5] L. Chomaz, I. Ferrier-Barbut, F. Ferlaino, B. Laburthe-Tolra, B. L. Lev, and T. Pfau, Dipolar physics: A review of experiments with magnetic quantum gases, arXiv preprint arXiv:2201.02672 (2022).
[6] T. Lahaye, C. Menotti, L. Santos, M. Lewenstein, and T. Pfau, The physics of dipolar bosonic quantum gases, Reports on Progress in Physics **72**, 126401 (2009).
[7] M. A. Baranov, M. Dalmonte, G. Pupillo, and P. Zoller, Condensed matter theory of dipolar quantum gases, Chemical Reviews **112**, 5012 (2012).
[8] S. Müller, J. Billy, E. Henn, H. Kadau, A. Griesmaier, M. Jona-Lasinio, L. Santos, and T. Pfau, Stability of a dipolar bose-einstein condensate in a one-dimensional lattice, Physical Review A **84**, 053601 (2011).
[9] S. Baier, M. J. Mark, D. Petter, K. Aikawa, L. Chomaz, Z. Cai, M. Baranov, P. Zoller, and F. Ferlaino, Extended bose-hubbard models with ultracold magnetic atoms, Science **352**, 201 (2016).
[10] B. Gadway and B. Yan, Strongly interacting ultracold polar molecules, Journal of Physics B: Atomic, Molecular and Optical Physics **49**, 152002 (2016).
[11] S. A. Moses, J. P. Covey, M. T. Miecnikowski, D. S. Jin, and J. Ye, New frontiers for quantum gases of polar molecules, Nature Physics **13**, 13 (2017).
[12] A. Browaeys and T. Lahaye, Many-body physics with individually controlled rydberg atoms, Nature Physics **16**, 132 (2020).
[13] R. Gupta, J. J. McClelland, P. Marte, and R. Celotta, Raman-induced avoided crossings in adiabatic optical potentials: observation of $\lambda/8$ spatial frequency in the distribution of atoms, physical review letters **76**, 4689 (1996).
[14] T. Schulze, B. Brezger, P. Schmidt, R. Mertens, A. Bell, T. Pfau, and J. Mlynek, Sub-100 nm structures by neutral atom lithography, Microelectronic engineering **46**, 105 (1999).
[15] C. Bradley, W. Anderson, J. J. McClelland, and R. Celotta, Nanofabrication via atom optics, Applied surface science **141**, 210 (1999).
[16] L. Caldwell and M. Tarbutt, Enhancing dipolar interactions between molecules using state-dependent optical tweezer traps, Physical Review Letters **125**, 243201 (2020).
[17] L. Caldwell and M. Tarbutt, General approach to state-dependent optical-tweezer traps for polar molecules, Physical Review Research **3**, 013291 (2021).

[18] M. Łącki, M. Baranov, H. Pichler, and P. Zoller, Nanoscale "dark state" optical potentials for cold atoms, Physical Review Letters **117**, 233001 (2016).

[19] S. Nascimbene, N. Goldman, N. R. Cooper, and J. Dalibard, Dynamic optical lattices of subwavelength spacing for ultracold atoms, Physical Review Letters **115**, 140401 (2015).

[20] A. Kruckenhauser, L. M. Sieberer, L. De Marco, J.-R. Li, K. Matsuda, W. G. Tobias, G. Valtolina, J. Ye, A. M. Rey, M. A. Baranov, *et al.*, Quantum many-body physics with ultracold polar molecules: Nanostructured potential barriers and interactions, Physical Review A **102**, 023320 (2020).

[21] Y. Wang, S. Subhankar, P. Bienias, M. Łącki, T.-C. Tsui, M. A. Baranov, A. V. Gorshkov, P. Zoller, J. V. Porto, and S. L. Rolston, Dark state optical lattice with a subwavelength spatial structure, Physical Review Letters **120**, 083601 (2018).

[22] M. McDonald, J. Trisnadi, K.-X. Yao, and C. Chin, Superresolution microscopy of cold atoms in an optical lattice, Physical Review X **9**, 021001 (2019).

[23] N. Lundblad, P. Lee, I. Spielman, B. Brown, W. Phillips, and J. Porto, Atoms in a radio-frequency-dressed optical lattice, Physical Review Letters **100**, 150401 (2008).

[24] T.-C. Tsui, Y. Wang, S. Subhankar, J. V. Porto, and S. L. Rolston, Realization of a stroboscopic optical lattice for cold atoms with subwavelength spacing, Physical Review A **101**, 041603 (2020).

[25] G. Ritt, C. Geckeler, T. Salger, G. Cennini, and M. Weitz, Fourier synthesis of optical potentials for atomic quantum gases, Physical Review A **74**, 063622 (2006).

[26] R. Anderson, D. Trypogeorgos, A. Valdés-Curiel, Q.-Y. Liang, J. Tao, M. Zhao, T. Andrijauskas, G. Juzeliūnas, and I. Spielman, Realization of a deeply subwavelength adiabatic optical lattice, Physical Review Research **2**, 013149 (2020).

[27] L. Förster, M. Karski, J.-M. Choi, A. Steffen, W. Alt, D. Meschede, A. Widera, E. Montano, J. H. Lee, W. Rakreungdet, *et al.*, Microwave control of atomic motion in optical lattices, Physical Review Letters **103**, 233001 (2009).

[28] A. M. Kaufman, B. J. Lester, and C. A. Regal, Cooling a single atom in an optical tweezer to its quantum ground state, Physical Review X **2**, 041014 (2012).

[29] Spin-1/2 atoms and alkalis for detunings larger than the excited-state hyperfine splitting share the property that they have only a scalar and vector polarizability. In general, atoms have a vector or tensor polarizability when light scattering can change their angular momentum by $\hbar$ or $2\hbar$, respectively [62, 63].

[30] O. Mandel, M. Greiner, A. Widera, T. Rom, T. W. Hänsch, and I. Bloch, Coherent transport of neutral atoms in spin-dependent optical lattice potentials, Physical Review Letters **91**, 010407 (2003).

[31] B. Yang, H.-N. Dai, H. Sun, A. Reingruber, Z.-S. Yuan, and J.-W. Pan, Spin-dependent optical superlattice, Physical Review A **96**, 011602 (2017).

[32] P. Soltan-Panahi, J. Struck, P. Hauke, A. Bick, W. Plenkers, G. Meineke, C. Becker, P. Windpassinger, M. Lewenstein, and K. Sengstock, Multi-component quantum gases in spin-dependent hexagonal lattices, Nature Physics **7**, 434 (2011).

[33] J. de Hond, J. Xiang, W. C. Chung, E. Cruz-Colón, W. Chen, W. C. Burton, C. J. Kennedy, W. Ketterle, *et al.*, Preparation of the spin-mott state: a spinful mott insulator of repulsively bound pairs, Physical Review Letters **128**, 093401 (2022).

[34] B. Gadway, D. Pertot, R. Reimann, and D. Schneble, Superfluidity of interacting bosonic mixtures in optical lattices, Physical Review Letters **105**, 045303 (2010).

[35] N. Belmechri, L. Förster, W. Alt, A. Widera, D. Meschede, and A. Alberti, Microwave control of atomic motional states in a spin-dependent optical lattice, Journal of Physics B: Atomic, Molecular and Optical Physics **46**, 104006 (2013).

[36] D. McKay and B. DeMarco, Thermometry with spin-dependent lattices, New Journal of Physics **12**, 055013 (2010).

[37] If the Raman couplings are eliminated using an external magnetic field, it breaks the symmetry of the $m_J = \pm 8$ states and causes rapid dipolar relaxation in the $m_J = +8$ layer.

[38] Depending on detuning, this contrast doesn't fully translate into the ac Stark shift because of the scalar background polarizability due to the strong transition triplet at 421, 419 and 405 nm.

[39] M. Lu, S. H. Youn, and B. L. Lev, Spectroscopy of a narrow-line laser-cooling transition in atomic dysprosium, Physical Review A **83**, 012510 (2011).

[40] For technical reasons, the lifetime measurements presented in Fig. 2 are done at trap frequencies of $(\omega_x, \omega_y, \omega_z) = 2\pi \times (0.7, 0.7, 153)$ kHz and temperature of $T = 5.5$ μK. This leads to an oscillator length of $a_{\mathrm{HO}} = 20.2$ nm and a layer thickness of $\sigma_z = \sqrt{\frac{\sum_{n=0}^{\infty}(2n+1)e^{-n\hbar\omega_z/k_BT}}{\sum_{n=0}^{\infty}e^{-n\hbar\omega_z/k_BT}}}\frac{a_{\mathrm{HO}}}{\sqrt{2}} = \sqrt{\coth\left(\frac{\hbar\omega_z}{2k_BT}\right)}\frac{a_{\mathrm{HO}}}{\sqrt{2}} \approx 1.31 a_{\mathrm{HO}}/\sqrt{2} \approx 18.8 \pm 0.1$ nm, where k_B is the Boltmann constant, owing to thermal excitation into the higher axial vibrational levels.

[41] S. Subhankar, Y. Wang, T.-C. Tsui, S. Rolston, and J. V. Porto, Nanoscale atomic density microscopy, Physical Review X **9**, 021002 (2019).

[42] B. Renklioglu, B. Tanatar, and M. Oktel, Heat transfer through dipolar coupling: Sympathetic cooling without contact, Physical Review A **93**, 023620 (2016).

[43] C. Charalambous, M. A. Garcia-March, M. Mehboudi, and M. Lewenstein, Heat current control in trapped bose–einstein condensates, New Journal of Physics **21**, 083037 (2019).

[44] S. Ronen, D. C. Bortolotti, D. Blume, and J. L. Bohn, Dipolar bose-einstein condensates with dipole-dependent scattering length, Physical Review A **74**, 033611 (2006).

[45] N. Matveeva, A. Recati, and S. Stringari, Dipolar drag in bilayer harmonically trapped gases, The European Physical Journal D **65**, 219 (2011).

[46] C.-C. Huang and W.-C. Wu, Center motions of nonoverlapping condensates coupled by long-range dipolar interaction in bilayer and multilayer stacks, Physical Review A **82**, 053612 (2010).

[47] J. Seamons, C. Morath, J. Reno, and M. Lilly, Coulomb drag in the exciton regime in electron-hole bilayers, Physical Review Letters **102**, 026804 (2009).

[48] A. Pikovski, M. Klawunn, G. Shlyapnikov, and L. Santos, Interlayer superfluidity in bilayer systems of fermionic polar molecules, Physical review letters **105**, 215302 (2010).

[49] J. Eisenstein and A. MacDonald, Bose–einstein condensation of excitons in bilayer electron systems, Nature **432**, 691 (2004).

[50] Z. Meng, L. Wang, W. Han, F. Liu, K. Wen, C. Gao, P. Wang, C. Chin, and J. Zhang, Atomic bose–einstein condensate in twisted-bilayer optical lattices, Nature **615**, 231 (2023).

[51] C. Trefzger, C. Menotti, and M. Lewenstein, Pair-supersolid phase in a bilayer system of dipolar lattice bosons, Physical Review Letters **103**, 035304 (2009).

[52] A. Argüelles and L. Santos, Mott-insulator phases of non-locally coupled one-dimensional dipolar bose gases, Physical Review A **75**, 053613 (2007).

[53] D.-W. Wang, M. D. Lukin, and E. Demler, Quantum fluids of self-assembled chains of polar molecules, Physical Review Letters **97**, 180413 (2006).

[54] P. Köberle and G. Wunner, Phonon instability and self-organized structures in multilayer stacks of confined dipolar bose-einstein condensates in optical lattices, Physical Review A **80**, 063601 (2009).

[55] A. Macia, G. Astrakharchik, F. Mazzanti, S. Giorgini, and J. Boronat, Single-particle versus pair superfluidity in a bilayer system of dipolar bosons, Physical Review A **90**, 043623 (2014).

[56] D. Hufnagl and R. E. Zillich, Stability and excitations of a bilayer of strongly correlated dipolar bosons, Physical Review A **87**, 033624 (2013).

[57] A. Safavi-Naini, Ş. G. Söyler, G. Pupillo, H. R. Sadeghpour, and B. Capogrosso-Sansone, Quantum phases of dipolar bosons in bilayer geometry, New Journal of Physics **15**, 013036 (2013).

[58] C. M. Holland, Y. Lu, and L. W. Cheuk, On-demand entanglement of molecules in a reconfigurable optical tweezer array, Science **382**, 1143 (2023).

[59] Y. Bao, S. S. Yu, L. Anderegg, E. Chae, W. Ketterle, K.-K. Ni, and J. M. Doyle, Dipolar spin-exchange and entanglement between molecules in an optical tweezer array, Science **382**, 1138 (2023).

[60] L. Christakis, J. S. Rosenberg, R. Raj, S. Chi, A. Morningstar, D. A. Huse, Z. Z. Yan, and W. S. Bakr, Probing site-resolved correlations in a spin system of ultracold molecules, arXiv preprint arXiv:2207.09328 (2022).

[61] B. Yan, S. A. Moses, B. Gadway, J. P. Covey, K. R. Hazzard, A. M. Rey, D. S. Jin, and J. Ye, Observation of dipolar spin-exchange interactions with lattice-confined polar molecules, Nature **501**, 521 (2013).

[62] F. Le Kien, P. Schneeweiss, and A. Rauschenbeutel, Dynamical polarizability of atoms in arbitrary light fields: general theory and application to cesium, The European Physical Journal D **67**, 1 (2013).

[63] X. Cui, B. Lian, T.-L. Ho, B. L. Lev, and H. Zhai, Synthetic gauge field with highly magnetic lanthanide atoms, Physical Review A **88**, 011601 (2013).

[64] W. Lunden, L. Du, M. Cantara, P. Barral, A. O. Jamison, and W. Ketterle, Enhancing the capture velocity of a Dy magneto-optical trap with two-stage slowing, Physical Review A **101**, 063403 (2020).

[65] I. Shvarchuck, C. Buggle, D. S. Petrov, K. Dieckmann, M. Zielonkowski, M. Kemmann, T. G. Tiecke, W. von Klitzing, G. V. Shlyapnikov, and J. T. M. Walraven, Bose-einstein condensation into nonequilibrium states studied by condensate focusing, Phys. Rev. Lett. **89**, 270404 (2002).

[66] K. Hueck, N. Luick, L. Sobirey, J. Siegl, T. Lompe, and H. Moritz, Two-dimensional homogeneous fermi gases, Phys. Rev. Lett. **120**, 060402 (2018).

[67] P. L. Gould, G. A. Ruff, and D. E. Pritchard, Diffraction of atoms by light: The near-resonant kapitza-dirac effect, Physical Review Letters **56**, 827 (1986).

[68] W. Ketterle, D. S. Durfee, and D. M. Stamper-Kurn, *Making, probing and understanding Bose-Einstein condensates,* in Bose-Einstein condensation in atomic gases, Proceedings of the International School of Physics "Enrico Fermi", Course CXL, edited by M. Inguscio, S. Stringari, and C. E. Wieman (IOS Press, Amsterdam, 1999) pp. 67–176.

[69] F. Böttcher, M. Wenzel, J.-N. Schmidt, M. Guo, T. Langen, I. Ferrier-Barbut, T. Pfau, R. Bombín, J. Sánchez-Baena, J. Boronat, *et al.*, Dilute dipolar quantum droplets beyond the extended gross-pitaevskii equation, Physical Review Research **1**, 033088 (2019).

[70] F. Francesca, Observation of a rotonic 'stripe phase' in a dipolar Bose-Einstein condensate, Master's Thesis, Università di Pisa (2018).

[71] B. Pasquiou, G. Bismut, Q. Beaufils, A. Crubellier, E. Maréchal, P. Pedri, L. Vernac, O. Gorceix, and B. Laburthe-Tolra, Control of dipolar relaxation in external fields, Physical Review A **81**, 042716 (2010).

[72] P. Barral *et al.*, Can the dipolar interaction suppress dipolar relaxation?, manuscript in preparation.

[73] C. Ticknor, Two-dimensional dipolar scattering, Physical Review A **80**, 052702 (2009).

[74] Y. Tang, A. Sykes, N. Q. Burdick, J. L. Bohn, and B. L. Lev, s-wave scattering lengths of the strongly dipolar bosons dy 162 and dy 164, Physical Review A **92**, 022703 (2015).

[75] B. Esry, C. H. Greene, and J. P. Burke Jr, Recombination of three atoms in the ultracold limit, Physical review letters **83**, 1751 (1999).

[76] M. Anderlini, D. Ciampini, D. Cossart, E. Courtade, M. Cristiani, C. Sias, O. Morsch, and E. Arimondo, Model for collisions in ultracold-atom mixtures, Physical Review A **72**, 033408 (2005).

SUPPLEMENTARY MATERIALS

Sample preparation.— Typically, a Bose–Einstein condensate (BEC) with 5×10^4 ^{162}Dy atoms in the lowest Zeeman state $m_J=-8$ is prepared by first loading a 1064 nm crossed optical dipole trap (XODT) from the 626 nm spin-polarized magneto-optical trap [64]. Evaporative cooling is then performed in a magnetic field of 0.42 G by ramping down the depth of the XODT. The trap frequencies of the XODT at the end of evaporation are $(\Omega_x,\Omega_y,\Omega_z)=2\pi\times(149,43,136)$ Hz. The condensate fraction is about 45% and the temperature is 60 nK.

By following the sequence depicted in Fig. 1(d), approximately 4.2×10^4 atoms are subsequently loaded into the bilayer potential. Due to the partial condensation of the cloud and technical heating during the loading, we simply assume a Gaussian distribution in the transverse direction such that the atomic density is

$$n^{\pm}_{i,3\mathrm{D}}(\rho,z)=n_{0,3\mathrm{D}}e^{-\frac{1}{2}\left(i\frac{\lambda}{2\sigma_{\mathrm{ODT}}}\right)^2}e^{-\frac{1}{2}\left(\frac{\rho}{\sigma_\perp}\right)^2}e^{-\frac{1}{2}\left(\frac{z\pm s/2}{\sigma_z}\right)^2} \tag{S1}$$

where $i=0,\pm1,\pm2,\ldots$ is the index of the bilayer in the whole array, and the superscript $(\pm)$ denotes the σ_+ or σ_- layer. The transverse width (RMS value of x and y) is given by $\sigma_\perp=\sqrt{\frac{k_BT}{m\omega_\rho^2}}=3.0$ μm with $\omega_\rho=2\pi\times500$ Hz and $T=1.7$ μK. The RMS thickness σ_z relates to the oscillator length as $\sigma_z=a_{\mathrm{HO}}/\sqrt{2}$, therefore in the tight direction $\sigma_z=\sqrt{\frac{\hbar}{2m\omega_z}}=14.9$ nm for $\omega_z=2\pi\times140$ kHz.

We measured σ_{ODT} by a matter-wave focusing technique [65, 66] which maps the spatial distribution into momentum distribution which is imaged after ballistic expansion. The procedure is the following: first, the XODT is turned back on and the bilayer potential is switched off suddenly after loading. After a quarter period of oscillation in the XODT, the initial spatial distribution is converted into a momentum distribution. Finally, atoms are released from the XODT for absorption imaging after ballistic expansion for time t. The width of the density distribution in the bilayer potential is related to the width of the cloud in the absorption image by $\sigma_{\mathrm{ODT}}=\sigma_{\mathrm{TOF}}/(\Omega_z t)=4.4$ μm. This value agrees with a value obtained by in-situ imaging of the bilayer using detuned imaging light. As a result, we populate about $4\sqrt{\pi}\sigma_{\mathrm{ODT}}/\lambda\approx42$ bilayers with 700 atoms in each layer of the central bilayer.

The peak density $n_{0,3\mathrm{D}}$ is expressed in terms of experimentally measured quantities as $n_{0,3\mathrm{D}}=3N^{\pm}_{\mathrm{tot}}/V_{\mathrm{eff}}$ with the effective trap volume of the whole bilayer array $V_{\mathrm{eff}}=12\pi^2\sigma_\perp^2\sigma_z(2\sigma_{\mathrm{ODT}}/\lambda)$. We assume balanced loading of the bilayers, so the peak 2D density $n_0=\sqrt{2\pi}\sigma_z n_{0,3\mathrm{D}}=1.3\times10^9$ cm^{-2} is the same in both layers initially.

The bilayers are thermal since the temperature increases to $T=1.7$ μK at the end of the loading procedure, which is above the critical temperature for 2D Bose-Einstein condensation of 0.5 μK. The energy scale set by the temperature of each layer is much larger than the transverse vibrational energy spacing $k_BT/\hbar\omega_x=k_BT/\hbar\omega_y\approx70\gg1$, but is small compared to the axial vibrational energy spacing $k_BT/\hbar\omega_z\approx0.25<1$. The axial thermal excitation is on the order of $e^{-\hbar\omega_z/k_BT}=0.02$ (and 0.18 for the heated layer at 3.9 μK in the interlayer thermalization experiment).

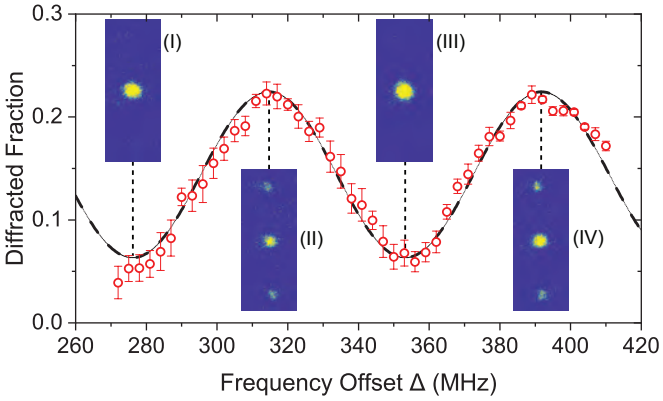

FIG. S1. **Characterization of the interlayer distance using Kapitza-Dirac diffraction.** The 1st-order fraction of the Kapitza-Dirac signals N_{+1}/N_{tot} versus relative detuning Δ with $m_J=-8$ Bose-Einstein condensates polarized along the **x** direction. The Kaptiza-Dirac signal vanishes at interlaced bilayer configurations (I) and (III), whereas it is maximized for overlapped bilayer configurations (II) and (IV).

Control and characterization of interlayer distances.— To control the distance between two layers, we shift the frequency of the σ_- optical standing wave, leading to a variable layer displacement due to the accumulated phase shift of the standing wave at the position of the atoms that is distance L away from the retro mirror. With $\delta f=80$ MHz tuning range of the σ_- optical frequency and 1.9 m of retro-path length, we are able to shift the σ_- layers by a distance $L\cdot\delta f/f=375$ nm with respect to the σ_+ layers, where f is the frequency of the 741 nm laser.

The distance is calibrated using a Kapitza-Dirac experiment [67] in which the diffraction patterns of atoms are used to reveal the structure of the pulsed optical standing waves. This is done with a BEC in the $m_J=-8$ Zeeman state polarized along the transverse direction **x** in a magnetic field of 1.3 G. After the preparation of the condensate, we simultaneously pulse on the two optical standing waves with the same intensity for $\tau=5$ μs, such that most of the population is in the the first order of the Kapitza-Dirac diffraction pattern. Since the transversely-polarized atomic spins see both circular polarizations as a superposition of (σ_-,π,σ_+) light with weights of (1, 2, 1), taking **x** as the quantization axis, the light-atom interaction Hamiltonian for the $m_J=-8$ state can be expressed as the superposition of two phase-shifted sinusoidal potentials of the same amplitudes $V_0(x,y)[\sin^2(kz)+\sin^2(kz+\phi)]$. Fig. S1 shows the typical first-order Kapitza-Dirac signals in the short pulse limit $V_0(x,y)\tau/h\ll1$. The result presents an oscil-

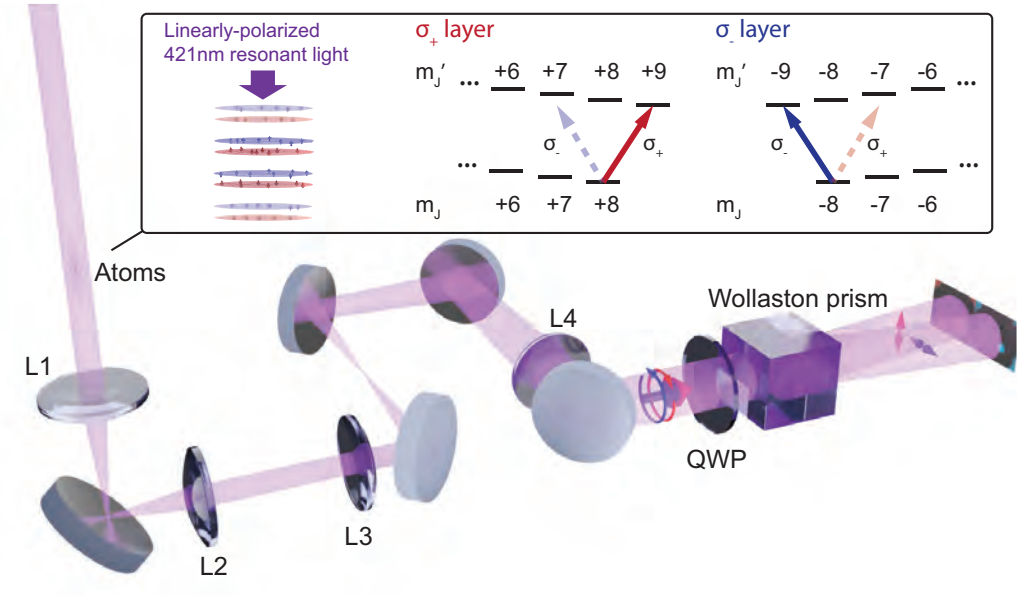

FIG. S2. **The spin-resolved absorption imaging scheme.** The atoms are exposed to linearly polarized light that is co-propagating with the bilayer optical beams and that is resonant with the 421 nm transition. After the relay lenses ($L1$ and $L2$) and the magnification lenses ($L3$ and $L4$), the σ_+ and σ_- components of the imaging light are separated using a quarter-wave plate (QWP) and a Wollaston prism. The spatially separated images of the σ_+ and the σ_- layers are recorded by a CMOS camera.

latory behavior as we vary the relative detuning Δ. When the bilayers are in an interlaced configuration ($\phi = \pi/2$), the first-order Kapitza-Dirac signal vanishes. When the bilayers are in an overlapped configuration ($\phi = 0$) the amplitude of the sinusoidal potential is maximized, corresponding to the strongest Kapitza-Dirac signal. The resulting oscillation period of the Kapitza-Dirac signal indicates the tuning sensitivity of the interlayer distance to be 4.7 nm/MHz with respect to the relative laser detuning Δ.

Spin-resolved imaging.— Our spin-resolved absorption imaging system operates in the weak saturation limit of the 421 nm cyling transition. It utilizes the big contrast of photon scattering rates of atoms in the stretched $m_J = \pm 8$ Zeeman states for two opposite circular polarizations of light. The resonant imaging light addressing the 421 nm transition is linearly polarized along $\mathbf{x}$, and propagates along the axial direction $\mathbf{z}$. Taking $\mathbf{z}$ as the quantization axis, the imaging light contains equal amount of σ_- and σ_+ polarization components. Due to the big difference between the Clebsch–Gordan coefficients for the $|J = 8, m_J = -8\rangle \rightarrow |J' = 9, m'_J = -9\rangle$ and the $|J = 8, m_J = -8\rangle \rightarrow |J' = 9, m'_J = -7\rangle$ electric dipole transitions, the σ_+ photons are predominantly scattered by the atoms in the σ_+ layer, whereas the σ_- photons are predominantly scattered by the atoms in the σ_- layer. The two polarization components are then spatially separated by a 1° angle via a quarter-wave plate and a Wollaston prism (see Fig. S2), leading to two nearly-independent imaging channels for the σ_+ and the σ_- layers on the camera. The duration of the imaging pulse is adjusted to reduce optical pumping which would lead to crosstalk between the two imaging channels.

Intra- and interlayer loss rates.— Here we provide the details of the model for determining the three-body loss rates for separated and overlapping layers. For technical reasons, these experiments were carried out with different parameters. Instead of loading from a BEC, the bilayers here were loaded from an ultracold thermal cloud at $T = 172$ nK with no condensate fraction. The thermal cloud follows a Gaussian density distribution with widths of $(\tilde{\sigma}_x, \tilde{\sigma}_y, \sigma_{\mathrm{ODT}}) = \sqrt{\frac{k_B T}{m}}(\frac{1}{\Omega_x}, \frac{1}{\Omega_y}, \frac{1}{\Omega_z}) = (3.1, 11.0, 3.5)\ \mu$m [68], and thus approximately 33 copies of the bilayer are created. The density distribution in each layer follows Eq. S1. The trap frequencies of the bilayer were $(\omega_x, \omega_y, \omega_z) = 2\pi \times (0.7, 0.7, 153)$ kHz, corresponding to an axial oscillator lengths of $a_{\mathrm{HO}} = \sqrt{\hbar/m\omega_z} = 20.2$ nm. The typical post-loading peak density is $n_{0,3\mathrm{D}} = 3.8 \times 10^{14}$ cm^{-3}.

For separated layers, the local density n decays by three-body loss according to $\mathrm{d}n/\mathrm{d}t = -\beta_{\mathrm{intra}} n^3$. By integrating over the cloud and layers we obtain the first term of the rate equation

$$\frac{dN_{\mathrm{tot}}}{dt} = -\beta_{\mathrm{intra}} \frac{N_{\mathrm{tot}}^3}{V_{\mathrm{eff}}^2} - \beta_{\mathrm{inter}} \frac{N_{\mathrm{tot}}^3}{V_{\mathrm{eff}}^2} e^{-\frac{1}{3}(\frac{s}{\sigma_z})^2} \qquad \text{(S2)}$$

with $V_{\mathrm{eff}} = 12\pi^2 \sigma_\perp^2 \sigma_z (2\sigma_{\mathrm{ODT}}/\lambda)$. The second term characterizes interlayer loss when the layers overlap with a rate constant β_{inter}. The prefactor $1/3$ in the exponent assumes three-body loss. For two-body loss, it would be $1/4$. Although two-body spin relaxation between

$m_J = \pm 8$ states becomes energetically possible when the layers partially overlap, it requires a higher-order process and should be negligible. The three-body recombination rate is proportional to the square of the density. Assuming that three-body collisions are independent of the spin state on a microscopic level, one would naively expect a fourfold increase of Γ_{3b} when the layers fully overlap — this is correct only in the case of a two-component Bose condensate. For spin-independent three-body collisions and a Bose condensate, we define $\beta = \beta_{\text{intra}}$. We then get $\beta_{\text{inter}} = 3\beta$. For thermal clouds we have $\beta_{\text{intra}} = g^{(3)}(0)\beta$ and $\beta_{\text{inter}} = 3g^{(2)}(0)\beta = \beta_{\text{intra}}$. and therefore an expected twofold increase of the loss rate for fully overlapping layers.

Fitting the initial loss rates $\dot{N}_{\text{tot}}/N_{\text{tot}}$ as a function of the interlayer distances s using Eq. (1) gives the intralayer three-body loss coeffcient $\beta_{\text{intra}} = 9.0 \times 10^{-28}$ cm^6/s, the interlayer three-body loss coefficient $\beta_{\text{inter}} = 4.8 \times 10^{-26}$ cm^6/s, and the RMS thickness of each layer $\sigma_z = 18.6$ nm $\approx 1.3 a_{\text{HO}}/\sqrt{2}$. The intralayer three-body loss coefficient is of the same order of magnitude compared to the results in previous works [69, 70] measured around 5 G magnetic fields away from Feshbach resonances.

Excitation and measurement of center-of-mass oscillations.— Oscillations of the σ_+ layer are excited using a circularly-polarized beam blue-detuned by 458 MHz from the 626 nm transition. The focus of the beam is misaligned along the **y** direction with respect to the atoms, causing a force that displaces the atoms along **y** due to the AC Stark shift gradient. The spin-selectivity of the beam due to its circular polarization guarantees that it predominantly addresses the σ_+ layer. By adiabatically ramping up the beam in 10 ms, we displace the σ_+ layer for various distances controlled by the final power of the beam. A center-of-mass oscillation is excited by suddenly switching off the beam.

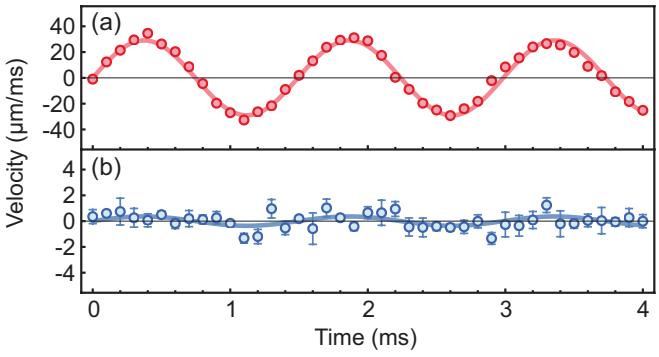

FIG. S3. **Characterization of the displacement beam crosstalk.** The first three cycles of center-of-mass oscillations caused by suddenly switching off the circularly-polarized 626 nm beam with (a) only the σ_+ layer loaded and (b) only the σ_- layer loaded. The resulting amplitudes of the σ_+ and σ_- layers are 29.0 ± 0.5 μm/ms and 0.36 ± 0.09 μm/ms respectively.

The displacement beam also displaces the σ_- layer owing to crosstalk, but 100 times less. The crosstalk could be observed only at much larger oscillation amplitudes than shown in Fig. 4 in the main text. We determined that the oscillation amplitude of the σ_- layer caused by the beam is 1.2(5)% compared to that of the σ_+ layer by measuring the amplitudes with only the σ_+ or σ_- layer loaded (see Fig. S3). This is consistent with the Clebsch-Gordon coefficients for the two polarizations.

When we explored the coupled oscillations for longer times and for larger amplitudes and separations, we found that the observations depended critically on a precise matching of the potentials of the two bilayers. Non-isotropic radial confinement could cause two-dimensional motion of the layers and Lissajous figure type orbits. Nevertheless, all observations showed an initial in-phase oscillation of the σ_- layer consistent with a frictional force.

Calculation of σ_{dd}.— The theoretical curves of the thermalization rate Γ_0 in Fig 3 use the distance-dependant interlayer dipolar cross section σ_{dd} of two atoms confined in two different layers. To compute this quantity, we use the Born approximation similar to Ref. [71, 72]. In the center-of-mass frame of two particles (labeled 1, 2) confined in two layers separated by distance s, the axial potential is reduced to a single harmonic oscillator potential $\hat{V}_{\text{HO}} = \frac{1}{2}\mu\omega_z^2(z-s)^2$, described by the relative axial coordinate $z = z_2 - z_1$ and a reduced mass $\mu = m/2$. Writing the transverse part of the wavefunction in the form of

$$\Psi(\boldsymbol{\rho}) = e^{ik\mathbf{u_i}\cdot\boldsymbol{\rho}} + e^{i\pi/4} f(k,\theta)\frac{e^{ik\rho}}{\sqrt{\rho}} \tag{S3}$$

leads to a scattering amplitude

$$f(k,\theta) = \frac{\mu}{\hbar^2}\frac{-1}{2\sqrt{2}\pi^{3/2}}\frac{1}{\sqrt{k}}\int \mathrm{d}q_z \mathcal{H}(-q_z)\mathcal{V}(\mathbf{q}) \tag{S4}$$

with $\mathbf{u_i}$ being the direction of the incident plane wave, $\mathbf{u}_\rho$ being the direction of the scattered wave, $\cos\theta = \mathbf{u_i}\cdot\mathbf{u}_\rho$ being the scattering angle, and $\mathbf{q} = k(\mathbf{u}_\rho - \mathbf{u_i}) + q_z\mathbf{u_z}$. Here $\mathcal{H}(q_z) = e^{-iq_z s - \sigma_z^2 q_z^2}$ is the Fourier transform of the harmonic oscillator ground state density of the two-particle potential $\hat{V}_{\text{HO}}$, and $\mathcal{V}(\mathbf{q}) = 4\pi\frac{\hbar^2}{\mu}a_{\text{dd}}(\frac{q_z^2}{|\mathbf{q}|^2} - 1)$ is the Fourier transform of the dipole-dipole interaction. Integrating over the angle θ leads to the 2D interlayer dipolar cross section

$$\sigma_{\text{dd}} = \int_0^{2\pi} \mathrm{d}\theta\, |f(k,\theta)|^2 \tag{S5}$$

This is the quasi-2D result presented in Fig. 3(a).

An analytic form of the cross section can be obtained in the pure 2D limit $\sigma_z = 0$ where the thickness of each layer is regarded as negligible. In this limit, the integral involved in the scattering amplitude can be simplified as $\int \mathrm{d}q_z e^{iq_z s}\left(\frac{q_z^2}{q_\rho^2+q_z^2} - 1\right) = -q_\rho \pi e^{-q_\rho s}$. Since

$q_\rho = k\,|\mathbf{u}_\rho - \mathbf{u}_\mathbf{i}|$, the integral for the 2D cross section is reduced to $\int_0^{2\pi} \mathrm{d}\theta q_\rho^2 e^{-2q_\rho s} = 2k^2 \int_0^{2\pi} \mathrm{d}\theta(1-\cos\theta)e^{-2\sqrt{2}ks\sqrt{1-\cos\theta}} \simeq 2k^2 \int_0^{\infty} \mathrm{d}\theta\theta^2 e^{-2ks\theta}$. For large interlayer distance $ks \gg 1$, the pure 2D dipolar cross section asymptotes to

$$\sigma_{\mathrm{dd}}^{\mathrm{2D}} = a_{\mathrm{dd}}^2 \frac{\pi}{k^2 s^3} \tag{S6}$$

This is the analytic result in Eq. 2 and the dashed curves in Fig. 3(a).

It is known that the Born approximation breaks down for overlapping layers $s = 0$ [73] due to the $1/r^3$ divergence of the dipole-dipole interaction. In order for the Born approximation to be valid, one requires the scattered part of the wavefunction to be small. A sufficient condition for this is

$$\frac{\mu}{\sqrt{2\pi}\hbar^2}\left|\int \mathrm{d}^2\rho_1 \frac{V_{\mathrm{dd}}(\boldsymbol{\rho}_1)}{\sqrt{k\,|\boldsymbol{\rho}_1|}}\right| \ll 1 \tag{S7}$$

This condition is fulfilled when $ks^3 \gg 1.13 a_{\mathrm{dd}}^2$. For our temperature range, this is satisfied when $s \gg 13$ nm.

Calculation of σ_c.— Eq. S4 can also be used to compute the effective quasi-2D cross-section arising from the contact s-wave interaction. For a scattering length a_s, the effective potential $\mathcal{V}_c(\boldsymbol{q}) = \frac{2\pi\hbar^2}{\mu} a_s$ gives

$$\sigma_c(k) = \frac{\pi a_c^2}{k\sigma_z^2} e^{-2s^2/\sigma_z^2} \tag{S8}$$

We use the low-field background value of $a_c = 5.9$ nm [74] in our calculations. The scattering length for collisions between -8 and +8 atoms is not known. The large three-body losses (which asymptotically scales with the forth power of the scattering length [75]) is an indication that the cross section for collisions between -8 and +8 atoms is 5 - 10 times larger. The shaded area in Figs. 3 and S4 indicates a range of a factor of 10.

Calculation of thermalization rate.— The thermalization rate Γ typically derives from the collision rate γ. The latter is given by the product of density n, the cross section σ and the average velocity $\bar{v}_r$. The thermalization rate is then usually obtained by dividing this quantity by the number of collisions necessary to reach thermalization. However in our case, although the dipolar potential in the $x-y$ plane is isotropic, the cross section $\sigma_{\mathrm{dd}}(k)$ is momentum dependent and highly anisotropic since the scattering amplitude $f(k,\theta)$ depends strongly on each of its variables. It is then necessary to take the full momentum distribution into account to compute the collision rate as in Ref. [76], which leads to the definition of an effective averaged cross section σ_{av} for collisions

$$\gamma = \frac{1}{2^{3/2}} n_{0,\mathrm{eff}} \bar{v}_r \sigma_{\mathrm{av}} \tag{S9}$$

where $n_{0,\mathrm{eff}} = n_0^{(-)} T^{(-)}/\bar{T}$ is the effective 2D peak density, and each three $\sqrt{2}$ factors comes from the averaging

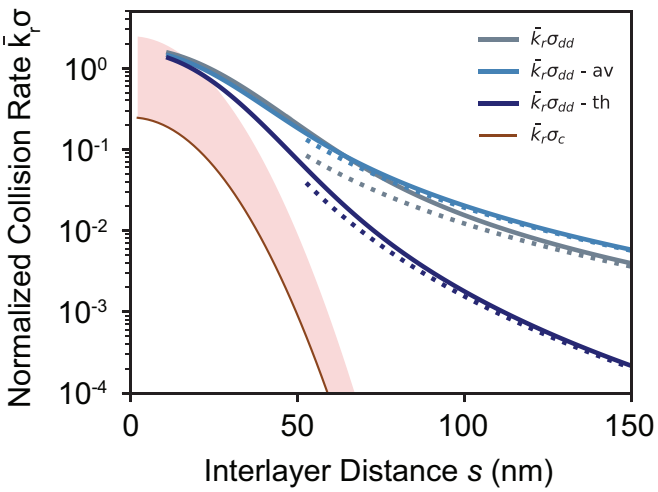

FIG. S4. **Calculation of normalized collision rates.** Dimensionless, density normalized collision rates $\bar{k}_r\sigma$ computed for contact and dipolar potential. $\bar{k}_r$ is the mean average momentum $\kappa\sqrt{\pi}/2$. The brown curve correspond to the contact interaction from Eq. S8 with the shaded red area indicating a 10 times larger cross section. The dashed gray, light blue and navy curves correspond to dipolar interaction in the pure 2D large-s approximation, Eq. S6, S13 and S14, respectively. The solid curves are for the quasi-2D cases, Eq. S5, S10 and S12, respectively.

of the rate along the two radial directions of the pancake and the discrete average over the stack of bilayer given the initial width of the loaded cloud. Introducing $\kappa = \sqrt{\frac{4k_B\bar{T}m}{\hbar^2}} = (2/\sqrt{\pi})(m\bar{v}_r/\hbar)$ we have

$$\sigma_{\mathrm{av}} = \frac{4}{\sqrt{\pi}}\frac{1}{\kappa^3}\int_0^\infty dk\sigma(k)k^2 e^{-k^2/\kappa^2} \tag{S10}$$

The thermalization rate Γ also incorporates the anisotropic redistribution of momentum between the two clouds. Forward scattering is less efficient for thermalization than scattering at larger angles. Therefore, we introduce the effective thermalization cross section σ_{th} such that

$$\Gamma = \frac{1}{2^{3/2}} n_{0,\mathrm{eff}} \bar{v}_r \sigma_{\mathrm{th}} \tag{S11}$$

with

$$\sigma_{\mathrm{th}} = \frac{2}{\sqrt{\pi}}\frac{1}{\kappa^5}\int_0^\infty dk k^4 e^{-k^2/\kappa^2}\int_0^{2\pi} d\theta(1-\cos\theta)\,|f(k,\theta)|^2 \tag{S12}$$

The definition is such that $\sigma_{\mathrm{av}} = \sigma$ for a momentum independent scattering amplitude. The ratio $\sigma_{\mathrm{av}}/\sigma_{\mathrm{th}}$ is the number of collision for thermalization. This ratio is 2/3 for an isotropic and momentum-independent scattering in 2D. For dipolar scattering, the ratio is much larger and depends on momentum and interlayer separation.

The contact interaction in 2D is a particular case where the ratio is 1, and the averaged cross section is also equal

to the non-averaged one taken at the mean relative momentum $\bar{k}_r = \kappa\sqrt{\pi}/2$, namely $\sigma_{c,\mathrm{av}}(\kappa) = \sigma_{c,\mathrm{th}}(\kappa) = \sigma_c(\bar{k}_r)$. The momentum-independent quantity $\bar{k}_r\sigma_c$ is plotted in Fig. S4. The impact of anisotopy is striking for the dipolar case. In the pure 2D and large distance $\kappa s \gg 1$ limits, the effective cross sections are

$$\sigma_{\mathrm{dd,\ av}} = a_{\mathrm{dd}}^2 \frac{2\pi}{\kappa^2 s^3} \tag{S13}$$

and

$$\sigma_{\mathrm{dd,\ th}} = a_{\mathrm{dd}}^2 \frac{3\pi}{\kappa^4 s^5} \tag{S14}$$

which are also plotted in Fig. S4. The cross section $\sigma_{\mathrm{dd,\ th}} \propto 1/s^5$ falls off with distance more rapdily than the dipolar potential $\propto 1/s^3$ since the larger the distance, the more pronounced forward scattering becomes. The red and black curves shown in Fig. 3(b) are Γ_c and Γ_{dd}, respectively.

Thermalization fit.— The thermalization rate Γ_{dd} depends on $n_0^- T^-/\bar{T}$, $\sigma_{\mathrm{dd,th}} \propto 1/k_r^4$ and $v_r \propto k_r$. The last two quantities purely depend on the relative momentum $k_r \propto \sqrt{\bar{T}}$ which is constant during the thermalization. The density scales with temperature as $n_0^- \propto N_{\mathrm{tot}}^-/T^-$, hence $n_0^- T^-/\bar{T} \propto N_{\mathrm{tot}}^-/\bar{T}$ which leaves Γ_{dd} independent of the temperature difference between the two layers $\Delta T = T^+ - T^-$. Therefore the only changing variable left out is the total atom number, and the differential equation for ΔT is

$$\frac{\mathrm{d}\Delta T}{\mathrm{d}t} = -\Gamma(t)\Delta T = -\Gamma_0 \frac{N_{\mathrm{tot}}^{\pm}(t)}{N_{\mathrm{tot}}^{\pm}(0)} \Delta T \tag{S15}$$

We observe losses attributed to three-body recombination with a timescale of 100 ms, and therefore we take them into account for fitting ΔT. Assuming a rate equation $\frac{\mathrm{d}N}{\mathrm{d}t} = -\Gamma_n N^3$ leads to the evolution of the temperature difference

$$\Delta T(t) = \Delta T_0 e^{\frac{\Gamma_0}{\Gamma_n N_0^2}\left(1-\sqrt{1+2\Gamma_n N_0^2 t}\right)} \tag{S16}$$

from which we can extract the interlayer thermalization rate Γ_0, plotted in Fig. 3.